Optik 161 (2018) 70–83

Contents lists available at ScienceDirect

Optik

journal homepage: www.elsevier.de/ijleo

Original research article

Reduced graphene oxide/platinum hybrid counter electrode assisted by custom-made triple-tail surfactant and zinc oxide/titanium dioxide bilayer nanocomposite photoanode for enhancement of DSSCs photovoltaic performance

A.B. Suriani[a,b,*], Fatiatun[a,b], A. Mohamed[b], Muqoyyanah[a,b], N. Hashim[a], M.S. Rosmi[a], M.H. Mamat[c,d], M.F. Malek[d,e], M.J. Salifairus[d], H.P.S. Abdul Khalil[f]

[a] *Nanotechnology Research Centre, Faculty of Science and Mathematics, Universiti Pendidikan Sultan Idris, 35900 Tanjung Malim, Perak, Malaysia*
[b] *Department of Physics, Faculty of Science and Mathematics, Universiti Pendidikan Sultan Idris, 35900 Tanjung Malim, Perak, Malaysia*
[c] *NANO-Electronic Centre (NET), Faculty of Electrical Engineering, Universiti Teknologi MARA (UiTM), 40450 Shah Alam, Selangor, Malaysia*
[d] *NANO-SciTech Centre (NST), Institute of Science (IOS), Universiti Teknologi MARA (UiTM), 40450 Shah Alam, Selangor, Malaysia*
[e] *Faculty of Applied Sciences, Universiti Teknologi MARA (UiTM), 40450 Shah Alam, Selangor, Malaysia*
[f] *Wood, Paper and Coating Division, School of Industrial Technology, Universiti Sains Malaysia, 11800 Pulau Pinang, Malaysia*

ARTICLE INFO

Article history:
Received 12 January 2018
Accepted 5 February 2018

Keywords:
Electrochemical exfoliation
Reduced graphene oxide/platinum hybrid
Counter electrode
Dye-sensitised solar cells

ABSTRACT

In this work, custom-made triple-tail sodium 1,4-bis(neopentyloxy)-3-(neopentyloxycarbonyl)-1,4-dioxobutane-2-silphonate (TC14) surfactant was used to assist exfoliation through electrochemical method for synthesis of graphene oxide (GO). A commercially available single-tail sodium dodecyl sulphate (SDS) surfactant was also utilised for comparison. Both synthesised GOs were reduced to produce reduced GO (rGO), which was fabricated into thin films through spray coating. The rGO thin film assisted by TC14 surfactant (TC14-rGO) with Pt nanoparticles was hybridised to improve electrical conductivity. The five different fabricated thin films were TC14-GO, TC14-rGO, SDS-rGO, Pt and TC14-rGO/Pt hybrid, which were used in dye-sensitised solar cells (DSSCs) as counter electrode (CE). Zinc oxide nanorods/titanium dioxide (ZnO NRs/TiO_2 bilayer) was used as photoanode and fabricated through a simple sol–gel immersion and squeegee method. Based on solar simulator measurement, TC14-rGO/Pt hybrid CE thin film exhibited the highest energy conversion efficiency of approximately 0.044% with the V_{oc}, J_{sc} and *FF* values of approximately 0.618 V, 0.163 mA/cm^2 and 0.387, respectively, compared with other fabricated CE materials. The combination of TC14-rGO/Pt hybrid CE and ZnO NRs/TiO_2 bilayer photoanode enhanced the DSSCs photovoltaic performance because of the high conductivity, low oxygen content, high quality and less agglomeration of thin rGO films as a result of improved exfoliation by triple-tail TC14 surfactant.

* Corresponding author at: Department of Physics, Faculty of Science and Mathematics, Universiti Pendidikan Sultan Idris, 35900 Tanjung Malim, Perak, Malaysia.
E-mail address: suriani@fsmt.upsi.edu.my (A.B. Suriani).

https://doi.org/10.1016/j.ijleo.2018.02.013
0030-4026/

1. Introduction

In the recent years, dye-sensitised solar cells (DSSCs) have been widely developed to replace conventional energy resources based on fossil fuel. DSSCs have attracted increasing attention in optoelectronic devices due to their low-cost production, low energy consumption, high energy conversion efficiency, simple fabrication process and environment friendly nature [1–3]. The DSSCs has four main components, namely, photoanode, dye, electrolyte and counter electrode (CE). Platinum (Pt) is the most popular material used as CE due to its high electrocatalytic activity to induce iodide/tri-iodide (I^-/I^{3-}) redox reaction and high energy conversion efficiency [4]. However, Pt is an expensive material, has limited bioavailability and is corrosive in liquid electrolyte. Thus, Pt needs to be reduced and replaced with other materials, such as graphene oxide (GO) and reduced GO (rGO). With their low-cost production, high optical transmittance, high electrical conductivity, large surface area [5,6] and high energy conversion efficiency, GO and rGO are suitable for DSSCs application [7]. GO can be synthesised by physical approaches, such as chemical vapor deposition (CVD) [8]. This method requires high energy consumption and uses high temperature, making it less efficient. Thus, this method is inapplicable for mass graphene production. Chemical approaches, such as Hummers method and electrochemical exfoliation, can be an alternative method to CVD [9]. However, Hummers method is expensive due to its high chemical consumption and leads to prolonged production and high defect level on the samples [10].

Electrochemical exfoliation can be a promising method for GO synthesis due to its low-cost production, simple preparation and environment-friendly and efficient process [9–11]. Sulphuric or acidic electrolytes determine the GO quality and must be considered for analysis. An approach using water-based electrolyte can also be utilised to achieve eco-friendly and safe GO production. A surfactant is required for water-based electrolytes to help intercalate exfoliation and weaken the Van der Waals interaction between graphite layers. In addition, surfactant is used to stabilise and help exfoliated GO dispersion [12]. Several surfactants commonly used in electrochemical exfoliation include commercially available single-tail sodium dodecyl sulphate (SDS) [9,11], sodium dodecylbenzene sulphonate (SDBS) [13], poly(sodium 4-styrenesulfonate) and double-tail sodium bis(3,5,5-trimethyl-1-hexyl) sulphosuccinate (AOT4) surfactant [14]. Mohamed et al. [15,16] utilised SDS, SDBS and AOT4 surfactants to disperse the multiwallled carbon nanotubes in natural rubber latex (NRL) and reduce the interfacial tension in the nanocomposites. Moreover, the SDS surfactant was successfully utilised to assist GO synthesis, where the produced GO is composited with NRL by one-step method and applied as an electrode for supercapacitor applications [17,18]. Meanwhile, the use of triple-tail surfactant, namely, sodium 1,4-bis (neopentyloxy)-3-(neopentyloxycarbonyl)-1,4-dioxobutane-2-silphonate (TC14) surfactant, exhibits optimal results for supercapacitor application of GO-assisted TC14–NRL nanocomposites. The custom-made triple-tail TC14 surfactant offers triple interaction during exfoliation, good dispersion and stabilisation of GO layers, thus yielding good GO quality. In this work, TC14 surfactant was used to assist GO synthesis and confer improved electrical properties of the fabricated CE thin films, thereby enhancing the DSSCs performance due to the CE role in facilitating electron transfer. For comparison, the commercially available single-tail SDS surfactant [6] was used to investigate its effect on GO production and fabrication of CE films.

Both synthesised GOs were reduced to produce rGO and decrease the oxygen (O) functional group within the produced GO formed during oxidation. Several reducing agents commonly used for reduction include protein bovine serum albumin [19], heparin [20], sugar [21] and polydiallydimethylammonium chloride [22]. Hydrazine hydrate is generally used as reducing agent due to its effectiveness for reducing O content compared with other reducing agents [23]. The synthesised and produced GO and rGO were then transferred in fluorine-doped tin oxide (FTO) substrate by using spray coating method to fabricate CE thin films. GO or rGO was also hybridised with Pt to enhance electrical properties. Gong et al. [24] reported the higher DSSCs efficiency of the Pt/rGO hybrid CE compared with pure Pt. Moreover, low amount of Pt in the hybrid film resulted in improved photovoltaic performance [24]. Thus, in this work, thin Pt coating was applied on the TC14-rGO films to investigate its effect in DSSCs photovoltaic performance. The existence of rGO from custom-made TC14 surfactant offered high surface area to TC14-rGO/Pt hybrid film, thereby improving the DSSCs performance compared with pristine Pt as DSSCs CE films.

Common materials fabricated as DSSCs photoanode are zinc oxide (ZnO) and titanium dioxide (TiO_2), which have wide band gap energies of approximately ~3.37 and ~3.20 eV, respectively [25–27]. The wide-band gap energy of the photoanode material is needed to absorb photon energy from sunlight and facilitate the electron movement from the conduction to valence band. Compared with TiO_2 (0.1–4 $cm^2\ V^{-1}\ s^{-1}$), ZnO (115–155 $cm^2\ V^{-1}\ s^{-1}$) exhibits higher mobility and developed as DSSCs photoanode material because of its high electron mobility [28,29]. Various morphology structures of successfully synthesised ZnO include nanorods (NRs) [30,31], nanowires (NWRs) [32], nanoflakes [33], tetrapods [34] and nanosheets [35]. For photoanode, the aligned ZnO NRs are commonly used as photoanode structure [30,31] due to its large surface area and good electron transport, offering low charge recombination and improved DSSCs photovoltaic performance [36,37]. To obtain high-quality ZnO nanostructures, several methods, such as sol–gel immersion [38], hydrothermal [39], chemical bath deposition [40] and CVD method [41], have been developed. Sol–gel immersion method is one of the most promising fabrication techniques for preparing ZnO thin film due to its simple fabrication, low-cost production and easy to control the ZnO growth suitable to be applied in mass ZnO production.

Aside from the high electron mobility of ZnO, its utilisation as photoanode in DSSCs application presents a lower energy conversion efficiency compared with TiO_2 due to its intrinsic instability caused by the agglomeration of Zn^{2+}/dye on the ZnO surface, affecting the electron injection [42]. TiO_2 materials, such as TiO_2-decorated ZnO NRs [43], TiO_2 nanoparticles/ZnO NRs [44], ZnO NRs array/TiO_2 nanoparticles [40], ZnO NRs/TiO_2 core shell [45], ZnO/TiO_2 core/shell NRs [46], ZnO NWRs/TiO_2 nanoparticles [47] and ZnO tetrapods/TiO_2 composite [34] were investigated to minimise the abovementioned problems.

The modification of the ZnO NRs/TiO_2 bilayer can be used to improve electron injection by reducing the agglomeration of Zn^{2+}/dye. Among TiO_2 nanostructures, nanoparticles are widely used as photoanode material due to their simple preparation, large surface area and high dye adsorption [48]. High dye molecule adsorption can enhance the absorption of incident light in the visible and near-infrared range, thereby enhancing electron excitation and DSSCs performance.

In this work, we propose for the first time the use of rGO prepared by custom-made triple-tail TC14 surfactant hybridised with Pt as CE thin film for DSSCs application. The TC14-rGO/Pt exhibited good CE performance for DSSCs application due to the thin layer of TC14-rGO and large surface area promoted by Pt coating. TC14 utilisation in GO synthesis offered good exfoliation, dispersion, stabilisation, less agglomeration of GO sheets and low oxygen (O) content. In addition, the novel photoanode fabrication method of ZnO NRs/TiO_2 bilayer fabricated by sol–gel immersion and squeegee method improved the photoanode performance. TiO_2 utilisation provided significant effect on dye adsorption, thus improving the DSSCs efficiency. This finding was supported by the high electron mobility promoted by ZnO NRs, enhancing the electron transfer.

2. Experimental details

2.1. Chemicals

For GO production using electrochemical exfoliation method, two pieces of graphite rods (99.99%, Good Fellow Company, Germany) with a diameter and length of 10 and 150 mm, respectively, were used as starting materials through electrochemical exfoliation method. Hydrazine hydrate (Merck, 80% soluble in water) was utilised as reducing agent in rGO production. FTO (Pro Global Tech, thickness 1.1 mm) was used as substrate. The ZnO/TiO_2 bilayer photoanode was fabricated by preparing MgZnO-seeded catalyst, growing ZnO NRs and applying TiO_2 nanoparticles. The 2-metoxyethanol ($C_3H_8O_2$), zinc acetate dehydrate ($Zn(CH_3COO)_2{\cdot}2H_2O$; 99.5% purity; EMSURE), magnesium nitrate hexahydrate ($Zn(NO_3)_3{\cdot}6H_2O$; 99% purity; Across Organic) and mono-ethanolamine (C_2H_7NO) were used to prepare the MgZnO-seeded catalyst. Meanwhile, the ZnO NRs were grown from ZnO solution by mixing zinc nitrate ($Zn(NO_3)_2$) and hexamethylenetramine (HMT). Furthermore, commercial titanium(IV) oxide nanopowder (Sigma Aldrich, particle size ~21 nm), titanium tetraisopropoxide (TTIP) and ethanol were used to fabricate TiO_2 nanoparticle photoanode. Ditetrabutylammonium *cis*-bis(isothiocyanato)bis(2,2′-bipyridyl-4,4′-dicarboxylato) ruthenium(II) (N719) dye (Sigma Aldrich) was prepared from acetonitrile, butyl alcohol and N719 (Solaronix). Electrolyte used dimethyl-propyl-benzinidiazole iodide (DPMII) prepared from veloron nitrile (Sigma-Aldrich), butyl pyridine (Sigma-Aldrich), iodolyte AN 50 (Solaronix), DMPII (Solaronix) and guanidine thiocyanate (QreC).

2.2. Fabrication of counter electrode

GO was synthesised through an electrochemical exfoliation method in water-based electrolyte solution containing both custom-made triple-tails TC14 and commercially available single-tail SDS surfactants [17]. The GO solution was synthesised by partially immersing two graphite rods in the 0.1 M electrolyte solution and connected to 7 V potential for 24 h synthesis at room temperature. Afterward, the GO was reduced by reduction to produce rGO where hydrazine hydrate was used as reducing agent. The approximate ratio of hydrazine hydrate and GO solution was 1:100, and this reduction was carried out at ~95 °C for 24 h. GO and rGO produced by custom-made triple-tails TC14 surfactant and rGO assisted by commercially available single-tail SDS surfactant were transferred using spray-coating method on the FTO substrate. The produced GO and rGO thin films were then annealed at 400 °C for 1 h in argon ambient. The pristine Pt and TC14-rGO/Pt hybrid thin films were fabricated by Pt nanoparticle coating at a thickness of ~10 nm via sputter-coater method.

2.3. Fabrication of photoanode

The procedures to fabricate ZnO NRs/TiO_2 bilayer as photoanode were as follows: preparing seeded catalyst, growing ZnO NRs and coating of TiO_2 nanoparticles on the surface of ZnO NRs. The MgZnO was used as the seeded catalyst and prepared by mixing 10 ml of solvent ($C_3H_8O_2$), 0.88 g of precursor ($Zn(CH_3COO)_2{\cdot}2H_2O$ and 0.44 g of dopant ($Zn(NO_3)_3{\cdot}6H_2O$). The 0.25 ml stabiliser (C_2H_7NO) was also then added in the solution. Afterward, MgZnO-seeded catalyst film was fabricated using spin-coating technique on a $2 \times 1\ cm^2$ FTO substrate at 3000 rpm for 60 s and annealed at 500 °C for 1 h.

The ZnO NRs were then grown on the MgZnO-seeded catalyst via sol–gel immersion method. ZnO solution of 0.05 M was prepared from 2.975 g of $Zn(NO_3)_2$ and 1.409 g of HMT into 200 ml of DI water. The ZnO NRs were grown in the water bath for 4 h immersion at 95 °C and then annealed for 1 h at 500 °C. Then, the TiO_2 nanoparticles were fabricated using squeegee method where the TiO_2 nanoparticles were coated on the surface of ZnO NRs (ZnO NRs/TiO_2 bilayer). The TiO_2 paste was prepared by mixing 3.5 g of commercial titanium(IV) oxide nanopowder, 0.5 ml of TTIP and 15 ml of ethanol. The coated film was subsequently annealed for 10 min at 150 °C in an oven and post-annealed for 1 h at 450 °C.

2.4. Fabrication of dye-sensitised solar cells

In this work, ZnO NRs/TiO_2 bilayer was used as photoanode, and five different CEs were fabricated, namely, TC14-GO, TC14-rGO, SDS-rGO, Pt and TC14-rGO/Pt hybrid. The photoanode film was initially immersed into 0.5 mM N719 dye for 24 h at room temperature. Meanwhile, the $\boldsymbol{I^-/I^{3-}}$ from DMPII was used as electrolyte. After ensembling, the electrolyte was injected

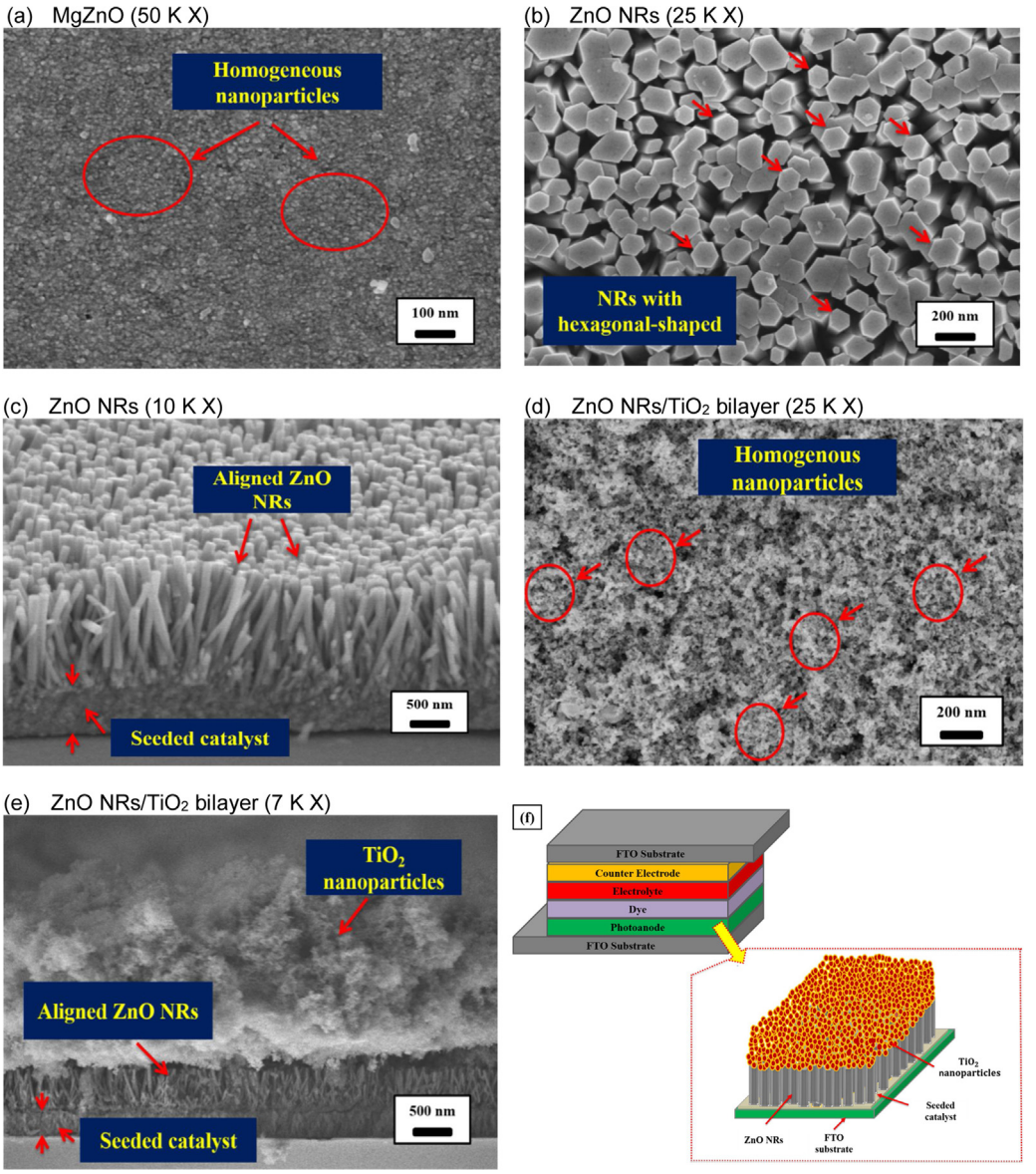

Fig. 1. FESEM images of (a) MgZnO-seeded catalyst, (b) top and (c) side views of ZnO NRs, (d) top and (e) side views of ZnO NRs/TiO_2 bilayer and (f) schematic diagram of DSSCs with ZnO NRs/TiO_2 bilayer as photoanode thin films.

from the edge between photoanode and CE. The photoanode and CE samples were then characterised using FESEM-Hitachi Su8020, EDX-Horiba EMAX, HRTEM-JEOL JEM 2100, micro-Raman spectroscopy (Renishaw InVia micro Raman System), X-ray diffraction (XRD) (D8 Advance), UV–vis spectroscopy (Cary 60) and four-point probe measurement (Keithley 2636A). Finally, the DSSCs performance was determined using a solar simulator and used a digital source meter (Oriel Sol1A) under illumination of simulated sunlight (AM 1.0).

3. Results and discussion

The field emission scanning electron microscopy (FESEM) images of fabricated ZnO NRs/TiO_2 bilayer as photoanode are presented in Fig. 1. Fig. 1(a) shows that the MgZnO-seeded catalysts distribute evenly all over the substrate with a homogeneous grain size diameter of 13–31 nm. The side view investigation showed that the fabricated MgZnO-seeded catalyst thickness was approximately 865–937 nm [Fig. 1(c)]. The top view of ZnO NRs grown on MgZnO-seeded catalyst exhibited high density of hexagonal-shaped ZnO with a diameter in the range of 92–107 nm [Fig. 1(b)]. Well-aligned ZnO NRs were observed from the side view of the sample, presenting the perpendicular direction on MgZnO-seeded catalyst with a thickness of approximately 1.51–1.81 μm [Fig. 1(c)]. Meanwhile, the top view of ZnO NRs/TiO_2 bilayer demonstrated

high density of TiO_2 nanoparticles with a diameter of 17–27 nm as shown in Fig. 1(d). The total thickness of ZnO NRs/TiO_2 bilayer was approximately 11.51–12.61 μm with a TiO_2 nanoparticle thickness of 9.70–10.80 μm [Fig. 1(e)]. The schematic diagram of fabricated DSSCs with ZnO NRs/TiO_2 bilayer as photoanode is demonstrated in Fig. 1(f).

FESEM images of fabricated CE thin films are shown in Fig. 2. The TC14-rGO [Fig. 2(a)] displayed wrinkles, sheet-like and thinner layer compared with TC14-GO and SDS-rGO due to low O content of 35.81% proven by energy-dispersive X-ray (EDX) analysis as presented in Fig. 2(b). Good interaction of triple-tail TC14 surfactant on the GO surface also affected the thin sheet layer of TC14-rGO [49]. The wrinkled structure of TC14-rGO was due to oxygen reaction sites isolated during reduction [50]. Meanwhile, thick layer was shown by TC14-GO affected by the high oxygen functional group that resulted during oxidation through electrochemical exfoliation method as demonstrated in Fig. 2(c) [51]. The TC14-GO also exhibited wrinkled structure on its surface due to successful oxidation. Higher atomic O percentages of TC14-GO compared with TC14-rGO was also proven by EDX analysis, presenting the O percentages of 51.28% and 35.81%, respectively, as shown in Fig. 2(d). Therefore, TC14-rGO exhibited better morphology structure and thin layer compared with TC14-GO. The SDS-rGO [Fig. 2(e)] demonstrated agglomerated sheets and thicker layer compared with TC14-rGO, which also exhibited higher O

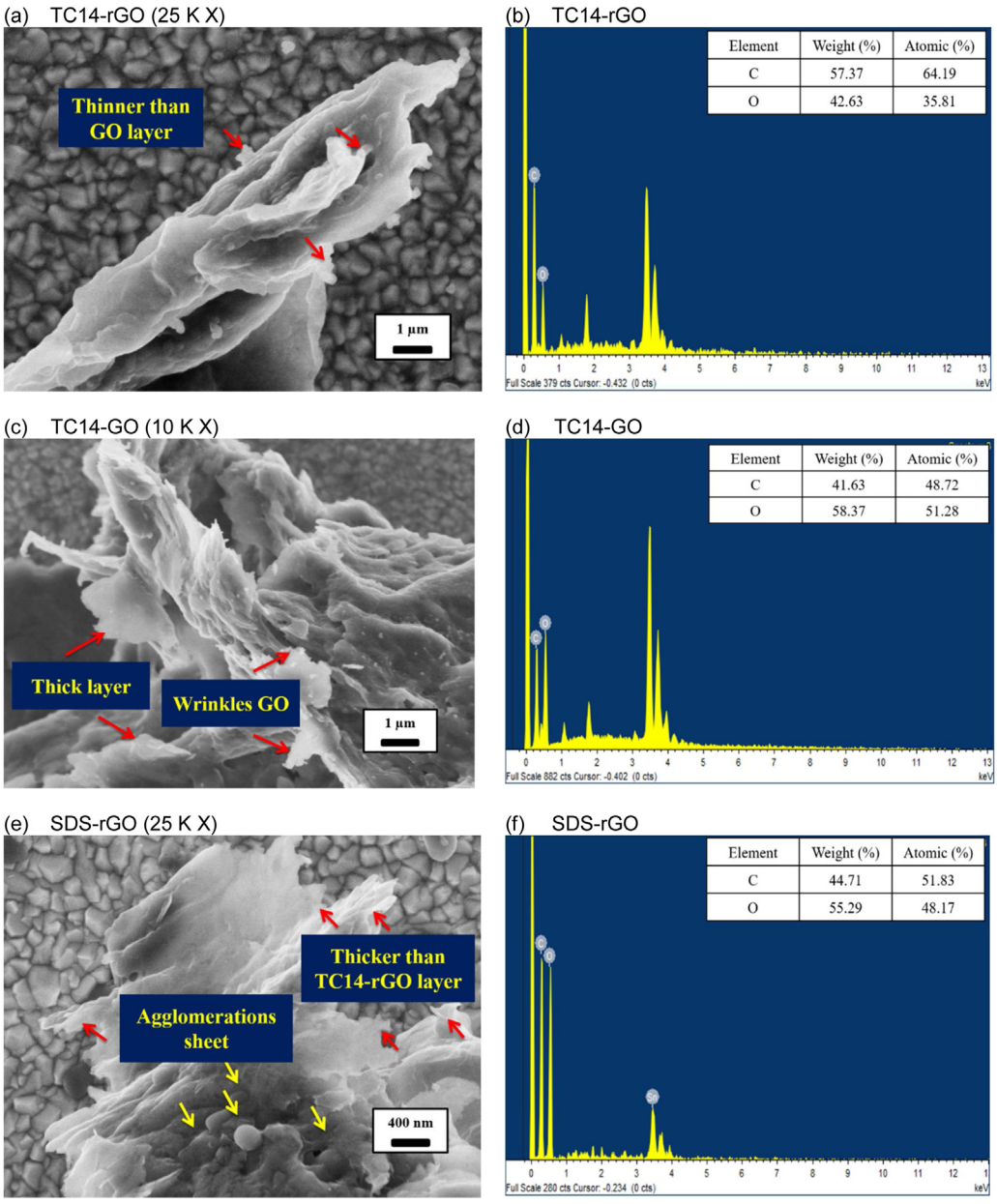

Fig. 2. FESEM images with EDX analysis of (a) and (b) TC14-rGO, (c) and (d) TC14-GO, (e) and (f) SDS-rGO, (g) and (h) Pt and (i) and (j) TC14-rGO/Pt hybrid as CE thin films.

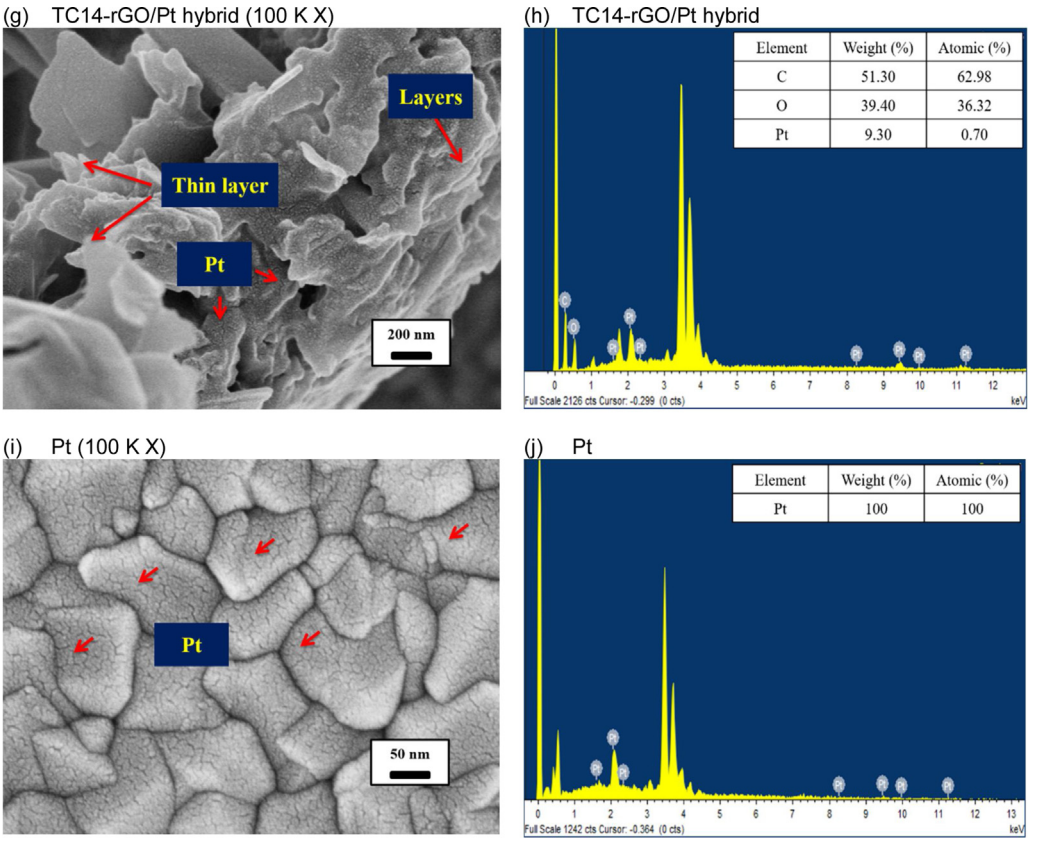

Fig. 2. (*Continued*)

content of 48.17% compared with TC14-rGO (35.81%) [Fig. 2(f)]. The single-tail SDS surfactant, providing a low exfoliation rate, dispersion and stabilisation on the produced GO, produced thick layer of SDS-rGO. After Pt was coated on TC14-rGO, the TC14-rGO/Pt hybrid exhibited homogeneous Pt nanoparticles distributed evenly all over the TC14-rGO layer as presented in Fig. 2(g). The homogeneous Pt nanoparticles were also seen in the pristine Pt [Fig. 2(i)]. EDX analysis was then used to confirm the existence of Pt in the samples, wherein the TC14-rGO/Pt [Fig. 2(h)] and pristine Pt [Fig. 2(j)] present the Pt atomic percentages of 0.70 and 100%, respectively.

Based on the high-resolution transmission electron microscopy (HRTEM) analysis, the TC14-rGO also possessed thinner layer (four layers), sheet-like and transparent layer than TC14-GO and SDS-rGO as demonstrated in Fig. 3(a and b). This result was also due to low O content in TC14-rGO caused by reduction [52] and less agglomeration promoted by triple-tail TC14 surfactant. Meanwhile, the TC14-GO [Fig. 3(c and d)] presented multilayer (seven layers) and thicker layer compared with TC14-rGO due to insertion of the oxygen functional group during oxidation [51]. The SDS-rGO [Fig. 3(e and f)] also showed multilayer (six layers) and thick sheets possibly affected by single-tail SDS surfactant, presenting a low exfoliation, dispersion, stabilisation and high agglomeration on the produced GO. These HRTEM images demonstrated that the thin layer was due to TC14-rGO and confirmed by FESEM images [Fig. 2(c)].

The micro-Raman spectra of ZnO NRs and CE thin films illustrated in Fig. 4 were used to investigate the crystallinity and defect of the samples [53]. The micro-Raman spectra of ZnO NRs [Fig. 4(a)] demonstrated four peaks, namely, E_2 high–E_2 low, A_1 (TO), E_2 (high) and E_1 (low), in the range of 200–800 cm^{-1}. The prominent peak was shown at 440 cm^{-1} [E_2 (high)], indicating good crystallinity and wurtzite structure in the ZnO NRs. Meanwhile, the low peak intensity at 333 cm^{-1} (E_2 high–E_2 low) and 382 cm^{-1} [A_1 (TO)] led to low defects in the ZnO NRs [54]. The ZnO NRs also presented low peak intensity at 587 cm^{-1} [E_1 (low)], indicating low oxygen vacancy and high crystallinity [54,55]. Fig. 4(b) shows that the micro-Raman spectra of TC14-rGO displayed a shifted peak of D- and G-bands from TC14-GO at 1354–1368 and 1584–1590 cm^{-1}, respectively, suggesting the successful reduction. The D-band presented the vibration of sp^3 carbon atom [56], whereas the G-band exhibited the layer number of sample during oxidation and also showed the vibration of sp^2 carbon atom [57]. The TC14-rGO also displayed high D-band peak intensity, which presents higher defects in this sample compared with SDS-rGO. Low G-band peak intensity of TC14-rGO demonstrated lower number of layer (four layers) than G-band peak intensity of TC14-GO (seven layers).

Based on the micro-Raman spectra, TC14-rGO showed higher I_D/I_G ratio (0.92) compared with TC14-GO (0.49) and SDS-rGO (0.75) that reveals the increasing number of sp^2 domain and amount of newly formed graphitic crystallites also indicating

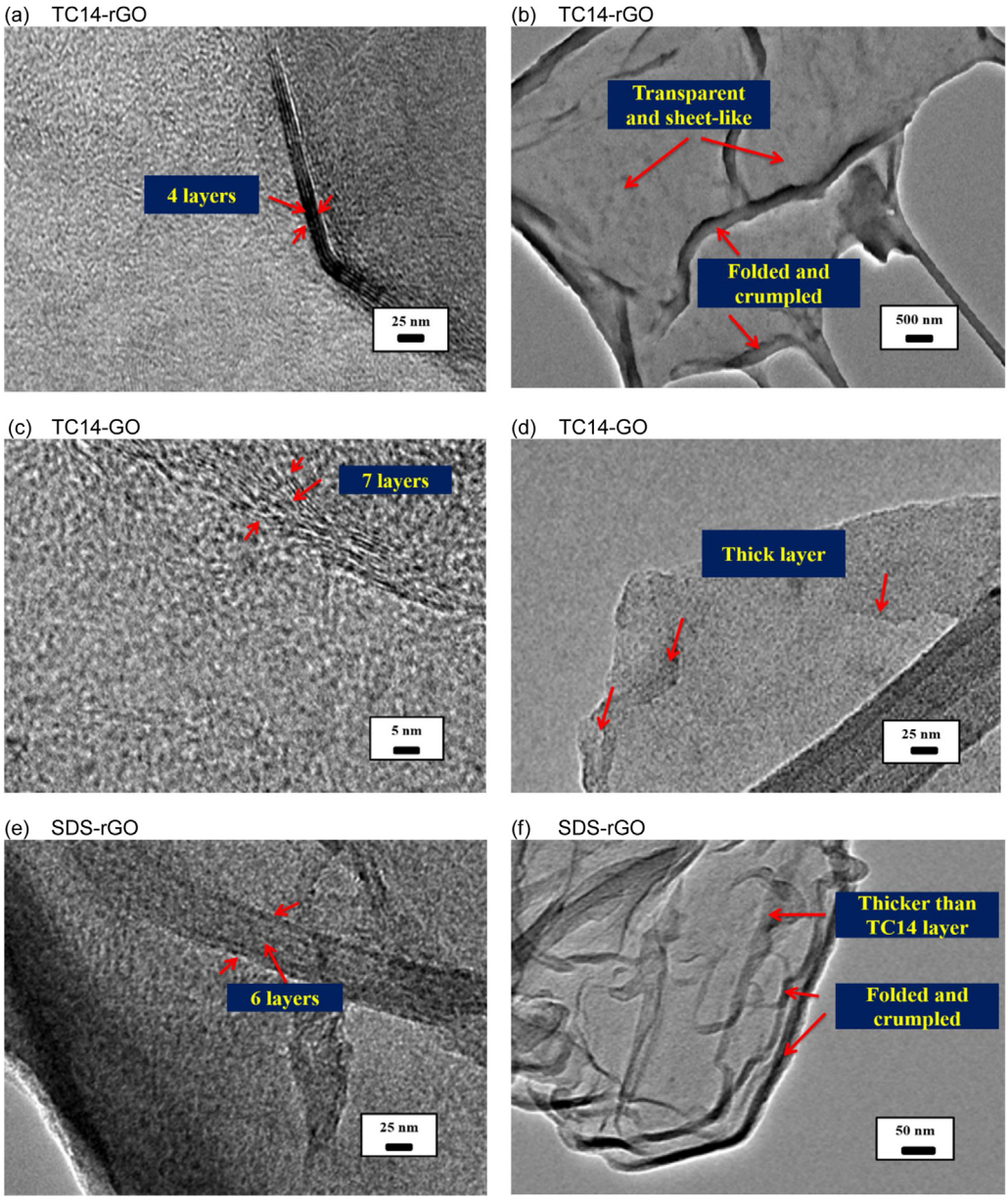

Fig. 3. HRTEM images of (a) and (b) TC14-rGO, (c) and (d) TC14-GO and (e) and (f) SDS-rGO as CE.

successful reduction [55,56]. This result was due to the decrement of the oxygen functional group during restoration of the π-conjugated systems and distortion of graphitic domains, which resulted during the reduction [58,59]. High I_D/I_G ratio of TC14-rGO also indicated the high amount of newly formed graphitic crystallites [60–62]. Meanwhile, the TC14-GO showed lower defects compared with TC14-rGO due to its low I_D/I_G ratio. Furthermore, the appearance of G^+ in the TC14-GO and SDS-rGO at 1623 and 1631 cm^{-1}, respectively, indicated the formation of polycrystalline domains [61]. The TC14-GO, TC14-rGO and SDS-rGO also demonstrated the 2D-band at 2713, 2766 and 2716 cm^{-1}, respectively, showing the number of GO and rGO layers [63]. A broad 2D-band at 265.93 cm^{-1} in the TC14-rGO presented high defect level also proven by high I_D/I_G ratio. Then, the TC14-rGO/Pt hybrid presented slightly higher I_D/I_G ratio (0.93) than pure TC14-rGO (0.92). The TC14-rGO/Pt hybrid also showed a shift of D-band from TC14-rGO of approximately 1368–1362 cm^{-1} due to the interaction between TC14-rGO sheets and Pt.

Fig. 5 shows the XRD patterns of the as-prepared ZnO NRs and ZnO NRs/TiO_2 bilayer. The ZnO NRs showed 10 peaks, which correspond to the (100), (002), (101), (102), (110), (103), (112), (201), (004) and (202) diffraction peaks, confirming the hexagonal-wurtzite structure of ZnO (PDF 01-078-4603). Among all the diffraction peaks, the most prominent and intense peak was shown at 34.8° (002), indicating the perpendicular direction of the as-grown ZnO to the substrate [64]. Higher

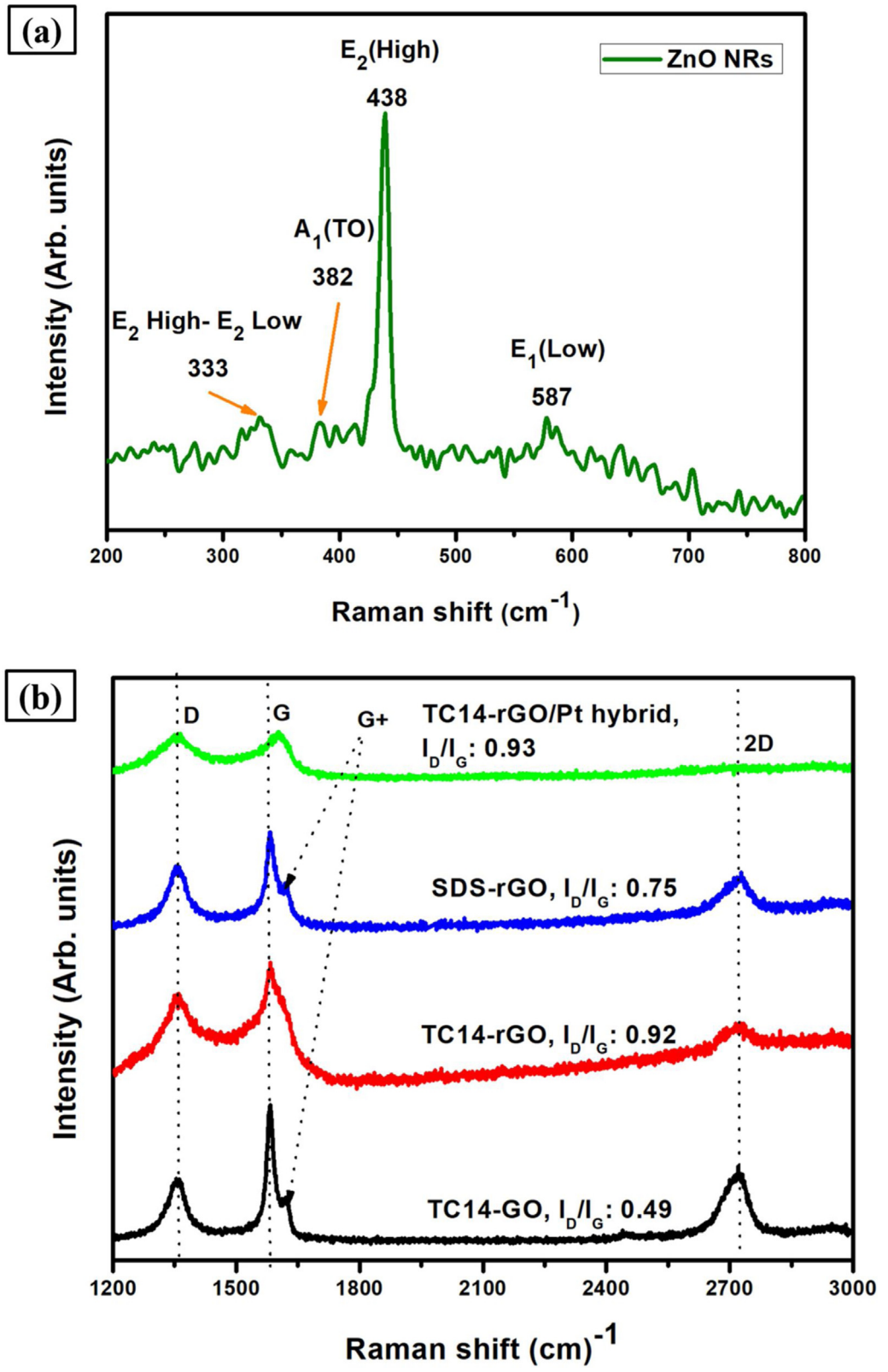

Fig. 4. Micro-Raman spectra of (a) ZnO NRs and (b) various CE materials.

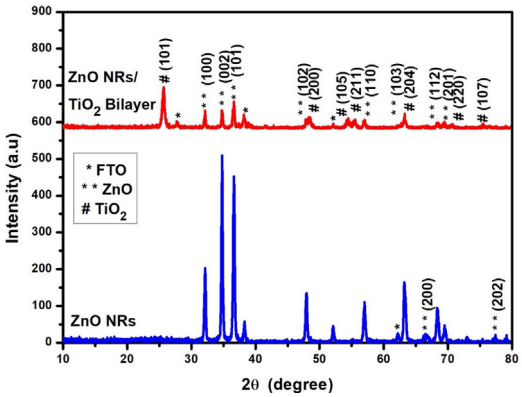

Fig. 5. XRD patterns of ZnO NRs and ZnO NRs/TiO_2 bilayer as photoanode materials.

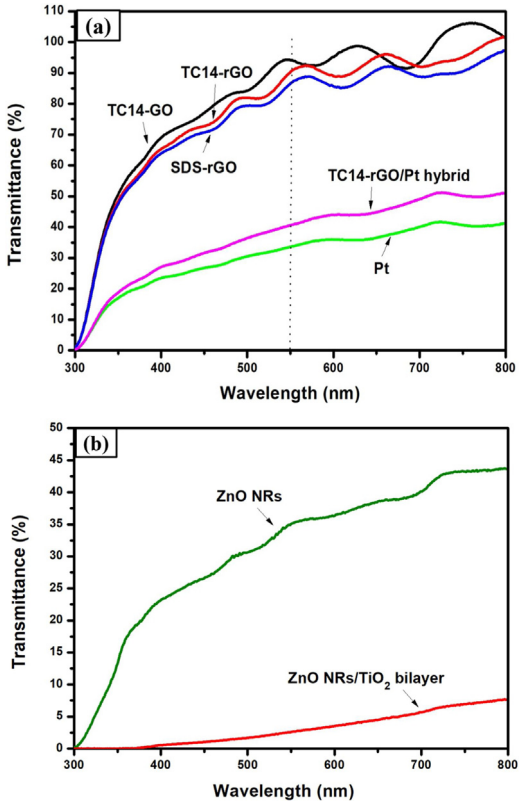

Fig. 6. UV–vis spectra of (a) various CE materials and (b) ZnO NRs and ZnO NRs/TiO_2 bilayer as photoanode thin films.

intensity and sharpness of (002) peak compared with other peaks indicated good crystallinity of ZnO NRs [53]. Meanwhile, the low intensity of other diffraction peaks was caused by imperfection of ZnO NR alignment on the substrate and also showed the increasing of grain boundary density in the sample. High crystallinity of ZnO NRs was also proven by low full width at half maximum (FWHM) calculated using Scherer's equation [65]. Based on calculation, the FWHM value of ZnO NRs was 0.21° with large crystallite size of 39 nm. Furthermore, the XRD pattern of ZnO NRs/TiO_2 bilayer showed both ZnO and anatase TiO_2 peaks. The XRD pattern of anatase TiO_2 nanoparticles presented mostly six peaks, which correspond to the (101), (004), (200), (105), (211) and (215) diffraction peaks (PDF 01-075-1537). The highest and prominent peak intensity of ZnO NRs/TiO_2 bilayer was observed along the *c*-axis (101) peak at 2θ–25.7°. The ZnO NRs/TiO_2 bilayer showed increment of FWHM and decrement of crystallite size to be approximately 0.36° and 22 nm, respectively.

Fig. 6 presents the optical properties (transmittance and band gap energy) of various CE thin films and photoanode based on UV–vis measurement. Based on the spectra [Fig. 6(a)], TC14-GO exhibited transmittance value of ~94%. Meanwhile, the TC14-rGO presented higher transmittance of ~92% compared with SDS-rGO (~88%) at λ = 550 nm in the range of 400–800 nm.

Table 1
Summary of transmittance and band gap energy of photoanode and various types of CE thin films.

Sample	Transmittance (%)	Band gap energy (eV)
ZnO NRs	2.6	3.34
ZnO NRs/TiO_2 bilayer	35	2.95
TC14-GO	94	4.03
TC14-rGO	92	3.98
SDS-rGO	88	4.01
Pt	35	3.95
TC14-rGO/Pt hybrid	42	3.92

Table 2
Summary of DSSCs performance with ZnO NRs/TiO_2 bilayer as photoanode and various CE thin films.

Sample	Open circuit voltage (V_{oc}) (V)	Short circuit current (J_{sc}) (mA/cm^2)	Fill factor (*FF*)	Energy conversion efficiency (η) (%)
TC14-GO	0.514	0.055	0.170	0.0055
TC14-rGO	0.512	0.070	0.157	0.0065
SDS-rGO	0.467	0.059	0.152	0.0048
Pt	0.623	0.141	0.431	0.0433
TC14-rGO/Pt hybrid	0.618	0.163	0.387	0.0445

High transmittance of TC14-rGO was due to smooth, transparent, and low O content caused by successful reduction. The triple-tail TC14 surfactant also provided less agglomeration, high dispersion and high quality of the produced GO synthesised using electrochemical exfoliation method. However, the transmittance of TC14-rGO decreased at ~42% when incorporated with Pt, affected by a low transmittance of pristine Pt (~35%). The transmittance of ZnO NRs and ZnO NRs/TiO_2 bilayer photoanode is shown in Fig. 6(b). The ZnO NRs/TiO_2 bilayer showed lower transmittance of ~2.6% compared with pure ZnO NRs (~35%) due to its thick layer of TiO_2 nanoparticles (9.70–10.80 μm) than pure ZnO NRs (1.51–1.81 μm).

From the transmittance value, the band gap energy of CE and photoanode materials were calculated using Tauc's plot with a linear extrapolation as shown in Fig. 7 [66]. For photoanode, the ZnO NRs/TiO_2 bilayer presented lower band gap energy (~2.95 eV) compared with pure ZnO NRs (~3.34 eV) as demonstrated in Fig. 7(a and b). This result was due to combination materials of ZnO and TiO_2 in the ZnO NRs/TiO_2 bilayer. Meanwhile, the TC14-rGO [Fig. 7(d)] showed lower band gap energy of ~3.98 eV compared with TC14-GO (~4.03 eV) [Fig. 7(c)] and SDS-rGO (~4.01 eV) [Fig. 7(e)], presenting high electrical conductivity of TC14-rGO. High band gap energy of TC14-GO was due to the high-oxygen functional group, which resulted during oxidation through electrochemical exfoliation method [67]. High band gap energy of SDS-rGO was affected by a single-tail SDS surfactant, which demonstrates a high agglomeration, low dispersion and stabilisation of produced GO. This phenomenon revealed that SDS-rGO presented slow electron movement in the CE for DSSCs application. Furthermore, the TC14-rGO/Pt hybrid [Fig. 7(g)] exhibited lower band gap energy of ~3.92 eV compared with pure TC14-rGO and pristine Pt of ~3.95 eV [Fig. 7(f)]. Therefore, low band gap energy of TC14-rGO/Pt hybrid suggested conductive film, leading to rapid electron movement. The summary of transmittance and band gap energy of photoanode and various types of CE thin films is presented in Table 1.

The electrical properties of photoanode and CE materials determined using four-point probe analysis are shown in Fig. 8. The ZnO NRs presented electrical conductivity of $\sim 1 \times 10^{-2}$ S cm^{-1} as shown in Fig. 8(a). Meanwhile, TC14-rGO exhibited better electrical conductivity of $\sim 5.6 \times 10^{-1}$ S cm^{-1} than TC14-GO ($\sim 4.3 \times 10^{-1}$ S cm^{-1}) and SDS-rGO ($\sim 5 \times 10^{-1}$ S cm^{-1}) [Fig. 8(b)]. High electrical conductivity of TC14-rGO was due to the low oxygen functional group in the produced rGO solution from successful chemical reduction [61]. The triple-tail TC14 surfactant also displayed good exfoliation, dispersion, stabilisation and high quality of produced GO, yielding good electrical properties. The electrical conductivity of TC14-rGO increased to $\sim 6.6 \times 10^{-1}$ S cm^{-1} when integrated with Pt, wherein pristine Pt exhibited high electrical conductivity of ~3.87 S cm^{-1}.

The current density–voltage (*J*–*V*) curves of DSSCs with ZnO NRs/TiO_2 bilayer as photoanode and various CE thin films are shown in Fig. 9. Among the CE materials, the TC14-rGO/Pt hybrid presented the highest energy conversion efficiency (0.0445%) with J_{sc}, V_{oc} and *FF* values of 0.163 mA/cm^2, 0.618 V and 0.387, respectively. This result was due to higher surface area of TC14-rGO/Pt hybrid than pristine Pt and better catalytic activity of TC14-rGO/Pt hybrid compared with pure TC14-rGO, TC14-GO and SDS-rGO. Table 2 shows that TC14-rGO/Pt hybrid presented the highest J_{sc} value due to low band gap energy (~3.92 eV) and high electrical conductivity ($\sim 6.6 \times 10^{-1}$ S cm^{-1}) [Figs. 7(g) and 8(b)]. The high J_{sc} value of the TC14-rGO/Pt hybrid indicated high catalytic activity during reduction of I_3^- to I^-. This phenomenon was caused by high I_D/I_G ratio of TC14-rGO/Pt hybrid, indicating high defect density on the surface and promoting several active sites for dye regeneration. Moreover, large surface area of TC14-rGO/Pt hybrid can optimally generate dye sensitiser after electron injection and accelerates electron transport, thus improving the DSSCs performance. The pristine Pt presented lower energy conversion efficiency of 0.0433% with J_{sc}, V_{oc} and *FF* values of 0.141 mA/cm^2, 0.623 V and 0.431, respectively, compared with TC14-rGO/Pt hybrid CE thin film. This result was due to low surface area and high band gap energy of Pt (~3.95 eV), wherein dye was minimally regenerated after electron injection and presented slow route of electrolyte regulation during DSSCs application [3]. This finding confirmed that TC14-rGO utilisation in TC14-rGO/Pt hybrid film improved the DSSCs photovoltaic performance compared with the conventional Pt.

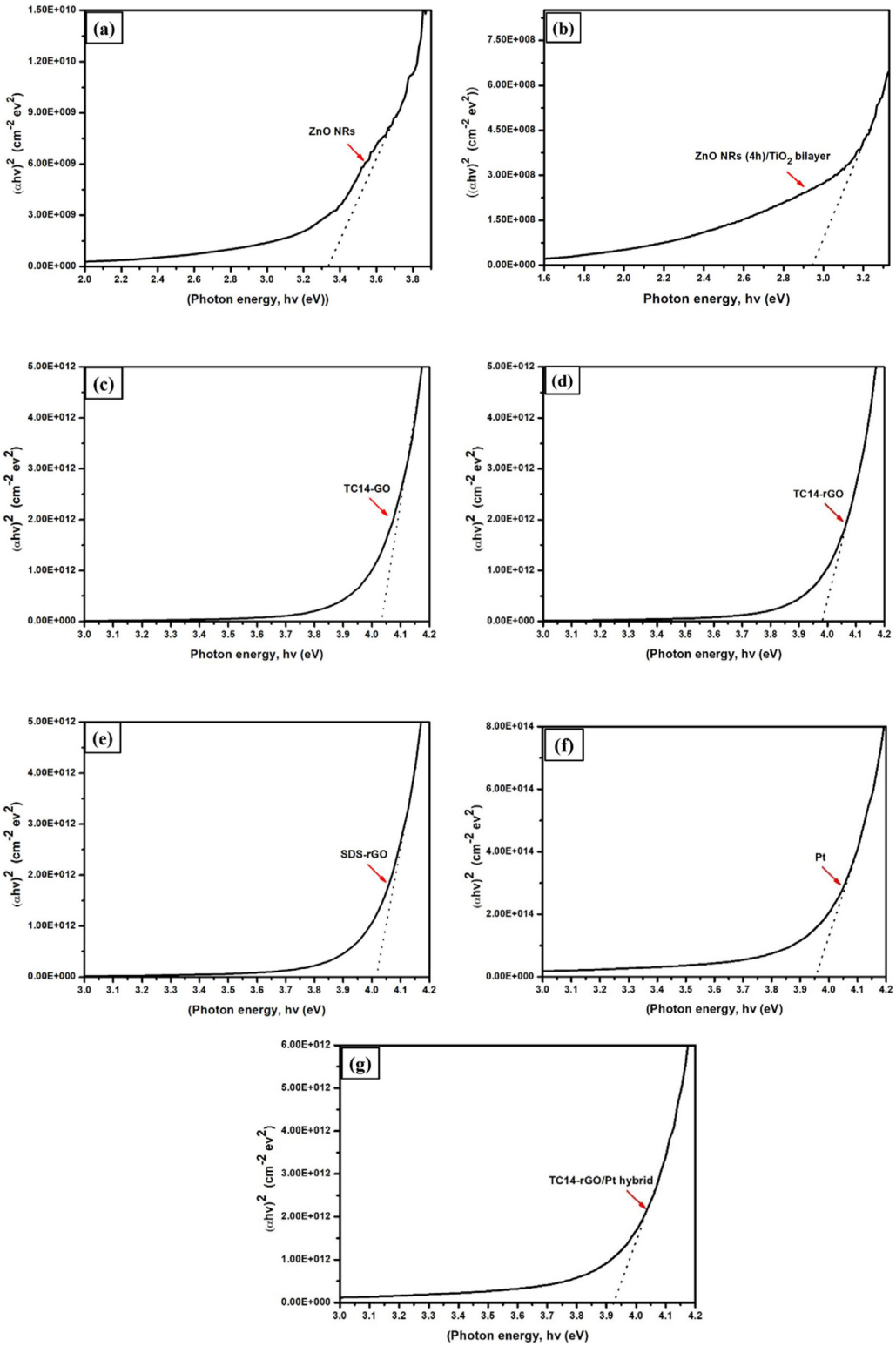

Fig. 7. Band gap energy of (a) ZnO NRs, (b) ZnO NRs/TiO_2 bilayer as photoanode, (c) TC14-GO, (d) TC14-rGO, (e) SDS-rGO, (f) Pt and (g) TC14-rGO/Pt hybrid as CE thin films.

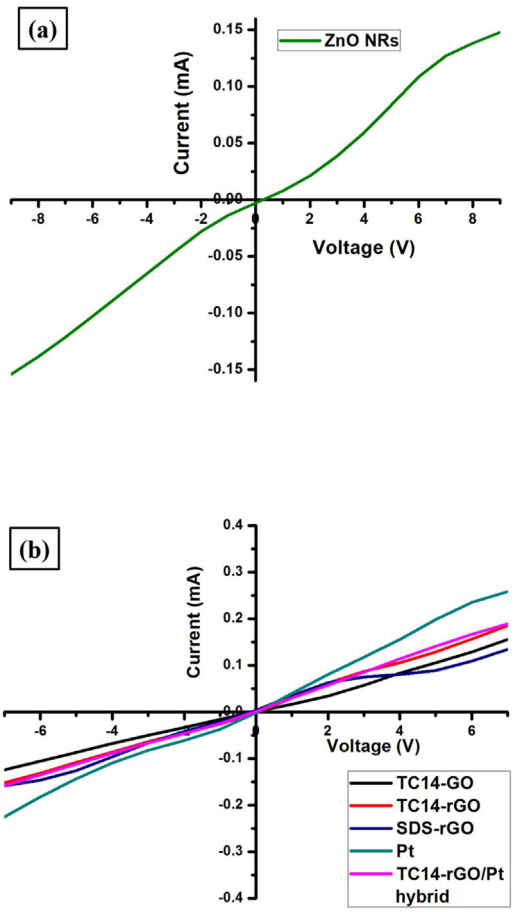

Fig. 8. *I–V* curve of (a) ZnO NRs and (b) various CE materials.

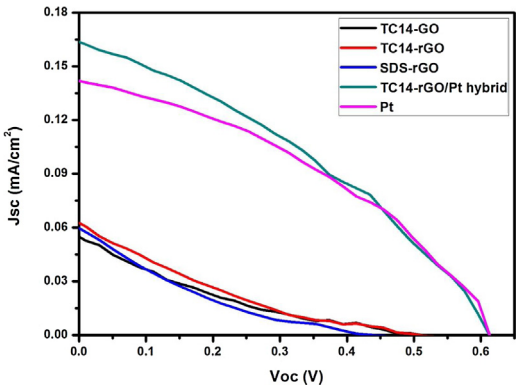

Fig. 9. *J–V* curve of DSSCs by using various CE materials and ZnO NRs/TiO_2 bilayer as photoanode thin films.

Meanwhile, TC14-rGO demonstrated higher energy conversion efficiency of 0.0065% and J_{sc} (0.070 mA/cm^2) compared with TC14-GO (0.0055% and 0.055 mA/cm^2) and SDS-rGO (0.0048% and 0.059 mA/cm^2), respectively. These results were due to high electrical conductivity ($\sim 5.6 \times 10^{-1}$ S cm^{-1}), low oxygen functional groups, thin layer (four layers) and low band gap energy ($\sim$3.98 eV) of TC14-rGO that accelerated electron movement and greatly improved the DSSCs performance. Moreover, the TC14-rGO exhibited stable rGO sheets, which can improve the diffusibility of the electrolyte for DSSCs application [68]. Meanwhile, lower energy conversion efficiency of SDS-rGO and TC14-GO compared with TC14-rGO were affected by agglomerated sheets of SDS-rGO, low electrical conductivity of SDS-rGO ($\sim 5 \times 10^{-1}$ S cm^{-1}) and TC14-GO ($\sim 4.3 \times 10^{-1}$ S cm^{-1}), thick layer of SDS-rGO (six layers) and TC14-GO (seven layers), enabling slow electron transport in CE for DSSCs application. The detailed results of DSSCs performance with various CE thin films are shown in Table 2.

High thickness of TiO_2 nanoparticles (9.70–10.80 μm) and ZnO NRs (1.51–1.81 μm) in the ZnO NRs/TiO_2 bilayer photoanode thin film presented important properties, wherein the TiO_2 nanoparticles were used to increase the dye adsorption of ZnO NRs/TiO_2 bilayer. The amount of adsorbed dye affected the amount of photo-exciton electron, further determining the J_{sc} value due to its role on incident photon absorption. High surface area of ZnO NRs and TiO_2 nanoparticles also caused low charge recombination in the ZnO NRs/TiO_2 bilayer photoanode for DSSCs application. Meanwhile, low band gap energy of ZnO NRs/TiO_2 bilayer (~2.95 eV) also presented high electrical conductivity ($\sim 5.64 \times 10^{-3}$ S cm^{-1}), suggesting fast electron transport in the photoanode and increased the DSSCs performance.

4. Conclusion

In summary, the TC14-rGO/Pt hybrid CE thin film shows the highest energy conversion efficiency of 0.0445% with V_{oc}, J_{sc} and *FF* value of 0.618 V, 0.163 mA/cm^2 and 0.387, respectively, compared with other CE thin films. The highest J_{sc} value of TC14-rGO/Pt hybrid was due to its high electrical conductivity ($\sim 6.6 \times 10^{-1}$ S cm^{-1}), low band gap energy (~3.92 eV) and large surface area, thus accelerating the electron transport. This finding was supported by the effectiveness of triple-tail TC14 surfactant during exfoliation, which yields less agglomeration, good dispersion and stabilisation of produced GO as initial solution for rGO production. In addition, the thick ZnO NRs/TiO_2 bilayer can optimally adsorb dyes, thus enhancing the light-harvesting efficiency. This finding indicated that the rGO assisted by custom-made TC14 surfactant improves the DSSCs performance. Therefore, this study can be used as a basis in the decrement of conventional Pt and development of composite between carbonaceous materials for CE in DSSCs application.

Acknowledgements

The authors are grateful to the TWAS-COMSTECH Joint Research Grant (Grant code: 2017-0001-102-11) and Fundamental Research Grand Scheme (Grant code: 2015-0154-102-02) for financial support.

References

[1] B. O'Regan, M. Grätzel, Nature 353 (6346) (1991) 737–740.
[2] H. Hug, M. Bader, P. Mair, T. Glatzel, Appl. Energy 115 (2014) 216–225.
[3] Y. Xue, J. Liu, H. Chen, R. Wang, D. Li, J. Qu, L. Dai, Chem. Int. Ed. 51 (2012) 12124–12127.
[4] G. Yue, J. Wu, Y. Xiao, M. Huang, J. Lin, J.Y. Lin, Electrochem. Acta 92 (2013) 64–70.
[5] D.W. Zhang, X.D. Li, H.B. Li, S. Chen, Z. Sun, X.J. Yin, S.M. Huang, Carbon 9 (2011) 0–6.
[6] A.B. Suriani, M.D. Nurhafizah, A. Mohamed, M.H. Mamat, M.F. Malek, M.K. Ahmad, A. Pandikumar, N.M. Huang, Opt. Int. J. Light Electron. Opt. 139 (2017) 291–298.
[7] N.G. Sahoo, Y. Pan, L. Li, S.H. Chan, Adv. Mater. 24 (15) (2012) 4203–4210.
[8] K.S. Kim, Y. Zhao, H. Jang, S.Y. Lee, J.M. Kim, K.S. Kim, J.H. Ahn, P. Kim, J.Y. Choi, B.H. Hong, Nature 457 (7230) (2008) 706–710.
[9] M. Alanyalioglu, J.J. Segura, J.O. Sole, N.C. Pastor, Carbon 50 (2011) 142–152.
[10] M.D. Disa, A.B. Suriani, S. Alfarisa, A. Mohamed, I.M. Isa, A. Kamari, N. Hashim, A.A. Aziz, M.R. Rusop, Adv. Mater. 1109 (2015) 55–59.
[11] A.B. Suriani, Muqoyyanah, A. Mohamed, M.H. Mamat, N. Hashim, I.M. Isa, M.F. Malek, M.I. Kairi, A.R. Mohamed, M.K. Ahmad, Opt. Int. J. Light Electron. Opt. 158 (2017) 522–534.
[12] A. Mohamed, T. Ardyani, S.A. Bakar, P. Brown, M. Hollamby, M. Sagisaka, J. Eastoe, Adv. Colloid Interface Sci. 230 (2016) 54–69.
[13] B.Q. Zeng, J. Cheng, L. Tang, X. Liu, Y. Liu, J. Li, Adv. Funct. Mater. 20 (2010) 3366–3372.
[14] S. Stankovich, R.D. Piner, X. Chen, N. Wu, T. Nguyen, R.S. Ruoff, J. Mater. Chem. 16 (2006) 155–158.
[15] A. Mohamed, A.K. Anas, A.B. Suriani, A.A. Aziz, M. Sagisaka, P. Brown, J. Eastoe, A. Kamari, N. Hashim, I.M. Isa, Colloid Polym. Sci. 292 (2014) 3013–3023.
[16] A. Mohamed, A.K. Anas, A.B. Suriani, T. Ardyani, M.W. Zin, S. Ibrahim, M. Sagisaka, P. Brown, J. Colloid Interface Sci. 445 (2015) 179–187.
[17] A.B. Suriani, M.D. Nurhafizah, A. Mohamed, I. Zainol, A.K. Masrom, Mater. Lett. 161 (2015) 665–668.
[18] A.B. Suriani, M.D. Nurhafizah, A. Mohamed, A.K. Masrom, M.H. Mamat, J. Mater. Sci. 52 (11) (2017) 6608–6619.
[19] J. Liu, S. Fu, B. Yuan, Y. Li, Z. Deng, J. Am. Chem. Soc. 132 (2010) 7279–7281.
[20] Y. Wang, P. Zhang, C.F. Liau, L. Zhan, Y.F. Li, C.Z. Huang, RSC. Adv. 2 (2012) 2322–2328.
[21] X. Xie, K. Zhao, X. Xu, W. Zhao, S. Liu, Z. Zhu, M. Li, Z. Shi, Y. Shao, J. Phys. Chem. C. 114 (2010) 14243–14250.
[22] S. Zhang, Y. Shao, H. Liao, M.H. Engelhard, G. Yin, Y. Lin, ACS Nano 5 (3) (2011) 1785–1791.
[23] L. Qiu, H. Zhang, W. Wang, Y. Chen, R. Wang, Appl. Surf. Sci. 319 (2014) 339–343.
[24] H.H. Gong, S.H. Park, S. Lee, S.C. Hong, Int. J. Precis. Eng. Manuf. 15 (6) (2014) 1193–1199.
[25] F.I.M. Fazli, M.K. Ahmad, C.F. Soon, N. Nafarizal, A.B. Suriani, A. Mohamed, M.H. Mamat, M.F. Malek, M. Shimomura, K. Murakami, Opt. Int. J. Light Electron. Opt. 140 (2017) 1063–1068.
[26] M.F. Malek, M.H. Mamat, Z. Khusami, M.Z. Sahdan, M.Z. Musa, A.R. Zainun, A.B. Suriani, N.D.M. Sin, S.B.A. Hamid, M. Rusop, J. Alloys Compd. 582 (2014) 12–21.
[27] M.F. Malek, M.H. Mamat, M.Z. Musa, Z. Khusami, M.Z. Sahdan, A.B. Suriani, A. Ishak, I. Saurdi, S.A. Rahman, M. Rusop, J. Alloys Compd. 610 (2014) 575–588.
[28] E.M. Kaidashev, M. Lorenz, H.V. Wenckstem, A. Rahm, H.-C. Semmelhack, K.-H. Han, G. Benndorf, C. Bundesmann, H. Hockmuth, M. Grundmann, Appl. Phys. Lett. 82 (22) (2003) 3901–3903.
[29] H. Tang, K. Prasad, R. Sanjinès, P.E. Schmid, F. Lévy, J. Appl. Phys. 75 (4) (1994) 2042–2047.
[30] Y. Wu, D. Liu, N. Yu, Y. Liu, H. Liang, G. Du, J. Mater. Sci. Technol. 29 (9) (2013) 830–834.
[31] M.F. Malek, M.H. Hafiz, T. Soga, S.A. Rahman, A.B. Suriani, A.S. Ismail, S.A.H. Alrokayan, H.A. Khan, M.R. Mahmood, Jpn. J. Appl. Phys. 55 (2016), 01AE15-1-6.
[32] J. Fan, Y. Hao, C. Munuera, M.G. Hernandez, F. Guell, E.M.J. Johansson, G. Boschloo, A. Hagfeldt, A. Cabot, J. Phys. Chem. C 17 (2013) 16349–16356.
[33] J. Mou, W. Zhang, J. Fan, H. Deng, W. Chen, J. Alloys Compd. 509 (3) (2011) 961–965.
[34] L.T. Yan, F.L. Wu, L. Peng, L.J. Zhang, P.J. Li, S.Y. Dou, T.X. Li, Int. J. Photoenergy (2012) (2012) 1–5.
[35] Z. Li, F. Gong, G. Zhou, Z. Wang, J. Phys. Chem. C 117 (2013) 6561–6566.
[36] V.V. Kislyuk, O.P. Dimitriev, J. Nanosci. Nanotechnol. 8 (1) (2008) 131–148.

[37] M.F. Malek, M.Z. Sadan, M.H. Mamat, M.Z. Musa, Z. Khusaimi, S.S. Husairi, N.D.M. Sin, M. Rusop, Appl. Surf. Sci. 275 (2013) 75–83.
[38] M.F. Malek, M.H. Mamat, M.Z. Sahdan, M.M. Zahidi, Z. Khusaimi, M.R. Mahmood, Thin Solid Films 527 (2013) 102–109.
[39] X. Fang, Y. Li, S. Zhang, L. Bai, N. Yuan, J. Ding, Sol. Energy 105 (2014) 14–19.
[40] H. Chou, H. Hsu, Solid State Electron. 116 (2016) 15–21.
[41] D.S. Kang, H.S. Lee, S.K. Han, V. Srivastava, E.S. Babu, S.K. Hong, M.J. Kim, J.H. Song, H. Kim, D. Kim, J. Alloys Compd. 509 (16) (2011) 5137–5141.
[42] Y. Lou, S. Yuan, Y. Zhao, P. Hu, Z. Wang, M. Zhang, L. Shi, D. Li, Chem. Eng. J. 229 (2013) 190–196.
[43] T. Guo, Y. Chen, L. Liu, Y. Cheng, X. Zhang, Q. Li, M. Wei, B. Ma, J. Power Sources 201 (2012) 408–412.
[44] Y.L. Xie, P.C. Lin, S.Q. Hu, Y.C. Lu, L. Li, H. Wang, J. Mater. Sci. Mater. Electron. 25 (2014) 2665–2670.
[45] G. Kia, L. Goh, H. Quang, T. Jiao, B. Tan, T. Hui, J. Solid State Chem. 214 (2014) 17–23.
[46] M. Wang, C. Huang, Y. Cao, Q. Yu, Z. Deng, Y. Liu, Z. Huang, J. Huang, Q. Huang, W. Guo, J. Liang, J. Phys. D Appl. Phys. 42 (2009), 155104-1-6.
[47] Y. Bai, H. Yu, Z. Li, R. Amal, G.Q. Lu, L. Wang, Adv. Mater. 24 (43) (2012) 1–7.
[48] S.F. Shaikh, R.S. Mane, B.K. Min, Y.J. Hwang, O.S. Joo, Sci. Rep. 6 (2016) 1–10.
[49] A. Kaniyoor, S. Ramaprabhu, J. Appl. Phys. 109 (2011), 124308-1-6.
[50] F. Barroso-bujans, S. Cerveny, R. Verdejo, J.J.D. Val, J.M. Alberdi, A. Alegria, J. Colmenero, Carbon 48 (2010) 1079–1087.
[51] F. Tavakoli, M. Salavati-Niasari, A. Badiei, F. Mohandes, Mater. Res. Bull. 63 (2015) 51–57.
[52] R. Devaraj, K. Karthikeyan, K. Jeyasubramanian, Appl. Nanosci. 3 (1) (2013) 37–40.
[53] F. Ahmed, S. Kumar, N. Arshi, M.S. Anwar, R. Prakash, Adv. Mater. Lett. 2 (3) (2011) 183–187.
[54] R. Devaraj, K. Karthikeyan, K. Jeyasubramanian, Appl. Nanosci. 3 (1) (2013) 37–40.
[55] Y. Zhang, M.K. Ram, E.K. Stefanakos, D.Y. Goswami, J. Nanomater. (2012) (2012) 1–22.
[56] R. Kumar, R.K. Singh, D.P. Singh, A.R. Vaz, R.R. Yadav, C.S. Rout, S.A. Moshkalev, Mater. Des. 122 (2017) 110–117.
[57] X. Chen, D. Pe, H. Wu, X. Zhao, J. Zhang, K. Cheng, P. Wu, S. Mu, Sci. Rep. 5 (16246) (2015) 1–10.
[58] A. Hessein, F. Wang, H. Masai, K. Matsuda, A.A. El-Moneim, Jpn. J. Appl. Phys. 55 (2016), 112301-1-8.
[59] S. Stankovich, D.A. Dikin, R.D. Piner, K.A. Kohlhaas, A. Kleinhammes, Y. Jia, Y. Wu, S.T. Nguyen, R.S. Ruoff, Carbon 45 (2007) 1558–1565.
[60] T.V. Khai, T.D. Lam, L. Van Thu, H.W. Kim, Mater. Sci. Appl. 6 (2015) 963–977.
[61] H. Liu, L. Zhang, Y. Guo, C. Cheng, L. Yang, L. Jiang, G. Yu, W. Hu, Y. Liu, D. Zhu, J. Mater. Chem. C 1 (2013) 3104–3109.
[62] L.C. Sim, K.H. Leong, S. Ibrahim, P. Saravanan, Mater. Chem. A 2 (2014) 5315–5322.
[63] C.T.J. Low, F.C. Walsh, M.H. Chakrabarti, M.A. Hashim, M.A. Hussain, Carbon 54 (2013) 1–11.
[64] V. Manthina, J.P.C. Baena, G. Liu, A.G. Agrios, J. Phys. Chem. C 116 (2012) 23864–23870.
[65] R. Shabannia, Prog. Nat. Sci. Mater. Int. 25 (2) (2015) 95–100.
[66] J. Tauc, R. Grigorovici, A. Vancu, Phys. Status Solidi 15 (627) (1966) 627–637.
[67] M.S. Poorali, M.M.B. Mohagheghi, J. Mater. Sci. Mater. Electron. 27 (1) (2015) 260–271.
[68] A.B. Suriani, M.D. Nurhafizah, A. Mohamed, A.K. Masrom, V. Shajwalla, R.K. Joshi, Mater. Des. 99 (2016) 174–181.